# TIME-ACCURATE SIMULATION OF FLOW PAST PZL W-3A "SOKÓŁ" (FALCON) HELICOPTER MAIN ROTOR IN FORWARD FLIGHT

Oskar SZULC[1], Piotr DOERFFER[1], Jerzy ŻÓŁTAK[2], Jacek MAŁECKI[3]

[1]*Institute of Fluid-Flow Machinery, Gdańsk, Poland;* [2]*Institute of Aviation, Warszawa, Poland;* [3]*PZL-Świdnik, Świdnik, Poland*
E-mail: Oskar.Szulc@imp.gda.pl

*Abstract*

The paper presents results of the numerical simulations based on the URANS approach and chimera overlapping grids technique of the main PZL W-3A "Sokół" (Falcon) helicopter rotor in forward flight conditions. The low-speed flight case models helicopter rotor as parallel to the ground keeping forward speed of approximately 100 km/h. Strong Blade-Vortex Interaction (BVI) is responsible for high level of vibration and noise. The high-speed (265 km/h) case reveals two main problems of modern helicopters: compressibility effects due to strong shock-wave boundary layer interaction on the advancing side and separation leading to dynamic stall on the retreating side of the rotor. The attempt is undertaken to correlate the results of the simulations with limited flight test data.

*Key words:* helicopter rotor, forward flight, chimera overlapping grid

## INTRODUCTION

The PZL W3 "Sokół" (Falcon) is a Polish medium-size, twin-engine, multipurpose helicopter manufactured by PZL-Świdnik (now AugustaWestland Świdnik) (fig. 1 – the W3-A version).



Fig. 1 PZL W3-A "Sokół" (Falcon) helicopter of the Tatra Volunteer Search and Rescue

This first helicopter fully designed and serially built in Poland is still in service (from 1987). The original main rotor design has served for more than 25 years and is still operating in hundreds of machines sold all over the world. The increasing significance of the fuel consumption and noise emission restrictions in form of the European Union regulations forces

the design of an improved version of the helicopter with increased performance and reduced fly-over noise. A completely new, 4-bladed main rotor (based on the ILH family of profiles (Kania W. et al, 2000)) for the modernized W3-A "Sokół" (Falcon) helicopter is designed, constructed by the "PZL Świdnik" S.A. company, verified experimentally through scale model wind tunnel tests by the Institute of Aviation (Poland) and tested numerically by the Institute of Fluid-Flow Machinery (Poland) (Doerffer P. et al., 2010 and 2011). In order to assess numerically the success of the new design it is necessary to compare with previous configuration based on the NACA family of profiles. The work described in the article contains results of the numerical simulations of the original, 4-bladed NACA rotor in forward flight conditions for the comparative study with an improved design based on ILH profiles, which has been developed recently at the Institute of Aviation and is still under research. This comparison will consists of the numerical analysis of the aerodynamics as well as aeroacoustics of both rotors.

A numerical simulation of the flow past a complete helicopter poses many challenges for the Computational Fluid Dynamics. Usually, the first approximation is to abandon the influence of the fuselage and tail rotor and to isolate the main rotor blades. The elastic deformation due to airloads is neglected in the overall picture as well. Still, the remaining task is computationally very demanding.

## GEOMETRICAL MODEL OF AN ISOLATED ROTOR

The geometrical characteristics of the main rotor of the PZL W3-A "Sokół" (Falcon) helicopter are summarized in tab. 1. The rotor consists of 4 blades (based on the NACA family of airfoils) having a radius of 7.85 m and linearly twisted from $0^o$ at the root ($z = 0.615$ m) up to $-12^o$ at the tip location. Apart from the root and tip area the chord is equal to 0.44 m.

| number of blades: | 4 |
|---|---|
| chord length [m]: | 0.44 |
| rotor radius [m]: | 7.85 |
| rotation direction: | clock-wise |

Tab. 1 Geometrical characteristics of the main rotor of the PZL W3-A "Sokół" (Falcon) helicopter

The rotor rotates in clock-wise direction as seen from above. The blades are equipped at the trailing edge with a trimming tab with deflection being unique and calibrated for each new set of blades. The real geometry of the rotor has been simplified only in the area close to the rotor hub (for $z < 0.989$ m). The constant deflection of all trimming tabs is assumed for the modelled blades as well. The final geometry used for numerical simulations is depicted in fig. 2. Three close-ups present in more details the simplified shape of the root area of the blade and unmodified rounded tip and trimming surfaces.

In forward flight rotor blades not only rotate around the azimuth ($\psi$), but also pitch ($\theta(\psi)$) and flap ($\beta(\psi)$) (lead-lag motion is not considered here). The azimuth angle $\psi$ is assumed to be $0^o$ for the first blade when it is pointing in the direction opposite to the flight direction. In forward-flight the shaft normal plane is additionally inclined to the flight direction (inflow) with an angle $\gamma$. The resulting motions may be summarized in a form of a Fourier series using first harmonics:

$$\begin{aligned}
\text{pitching:} \quad & \theta\,[^o] = \theta_0 + \theta_1 \cos(\psi) + \theta_2 \sin(\psi), \\
\text{flapping:} \quad & \beta\,[^o] = \beta_0 + \beta_1 \cos(\psi) + \beta_2 \sin(\psi), \\
\text{shaft:} \quad & \gamma\,[^o] = const,
\end{aligned} \tag{1}$$

where $\theta_0$ – collective pitch, $\theta_1$ and $\theta_2$ – lateral and longitudinal cyclic coefficients, $\beta_0$ – coning angle measured at the flap hinge, $\beta_1$ and $\beta_2$ – longitudinal and lateral flapping coefficients, and $\gamma$ – a constant angle of inclination of the shaft normal plane to the flight direction. The distance from the rotation axis to the flap hinge is equal to 0.14 m. It is assumed that there is no shift between the feathering (pitch) axis and the rotation axis.
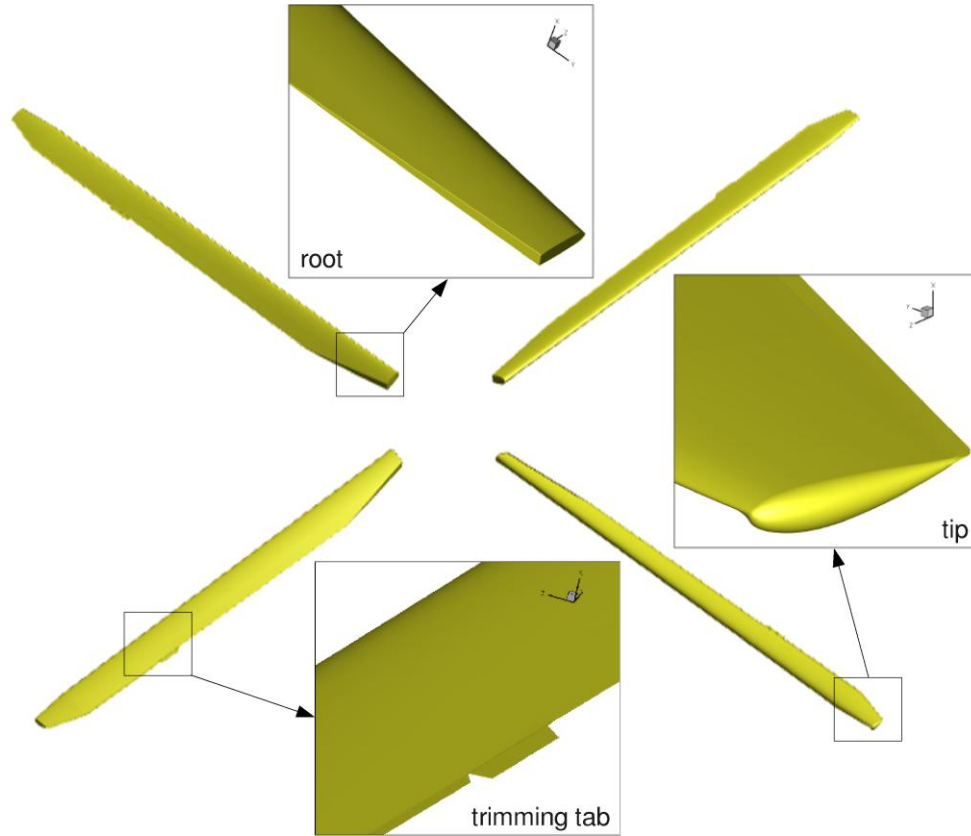


Fig. 2 Numerical model of the main rotor of the PZL W3-A "Sokół" (Falcon) helicopter

## CHIMERA OVERLAPPING GRID COMPONENTS

The main idea of the chimera technique (implemented in FLOWer code from DLR (Kroll et al., 2002)) is to generate easily grids for complex configurations by decomposing them into simple, independent parts (Schwartz, 2005). The only limitation is that all component meshes should overlap each other to allow inter-grid communication. All meshes are placed inside a simple background Cartesian grid. If any grid volume falls inside a solid body of the neighbouring component grid it is marked and excluded from the calculation process. The process of creation of "holes" has to ensure a sufficient overlap between meshes limiting interpolation errors during transfer of the flow data between grids. In case of rotors in forward flight the chimera overlapping grids technique allows for easy control of the rigid motion of the blades (translation, rotation, pitch and flap) preventing any grid deformation.

The component overlapped meshes for the PZL W3-A "Sokół" (Falcon) helicopter rotor has been generated using script-based (python) semi-automatic meshing within IGG software (Numeca International (2012)) and are summarized in tab. 2. Three component grids created for a single rotor blade (root, centre and tip) are placed within the background mesh. The remaining three blades are generated automatically. The application of the chimera technique (apart from the generation of component grids) requires creation of "holes" – simple structures designed to blank unneeded cells that fall into the geometry of the other components.

| grid component | number of blocks | number of volumes | designed $y^+$ |
|:---:|:---:|:---:|:---:|
| background | 1 x 32 | 1 x 10.35·10$^6$ | - |
| blade root | 4 x 13 | 4 x 1.19·10$^6$ | 1.0 |
| blade centre | 4 x 118 | 4 x 5.30·10$^6$ | 1.0 |
| blade tip | 4 x 19 | 4 x 1.08·10$^6$ | 1.0 |
| blade "hole" | 4 x 1 | - | - |
| total | 632 | 40.63·10$^6$ | 1.0 |

Tab. 2 Summary of the chimera overlapping grid components

The Cartesian background grid (fig. 3) is designed as a cuboid with dimensions of 16.4 R x 18.2 R x 18.2 R with uniform volumes (dimensions of 0.16 c x 0.16 c x 0.16 c) in the refined vicinity of the rotor blades and its wake. As a result the farfield surface is located at least 8.0 R from the rotor in every direction. Away from the rotor the grid spacing is more relaxed and stretched. 32 computational blocks contain 10.35 ·10$^6$ volumes (25% of the total number of cells). The background grid component undergoes only translation with forward flight velocity and a constant tilt by a shaft angle $\gamma$.
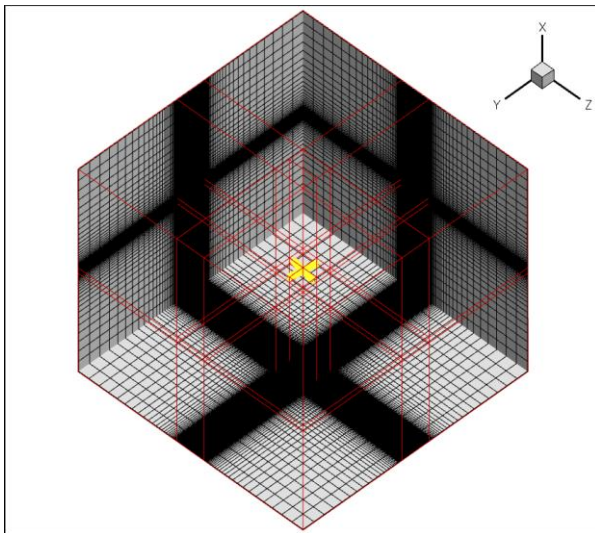


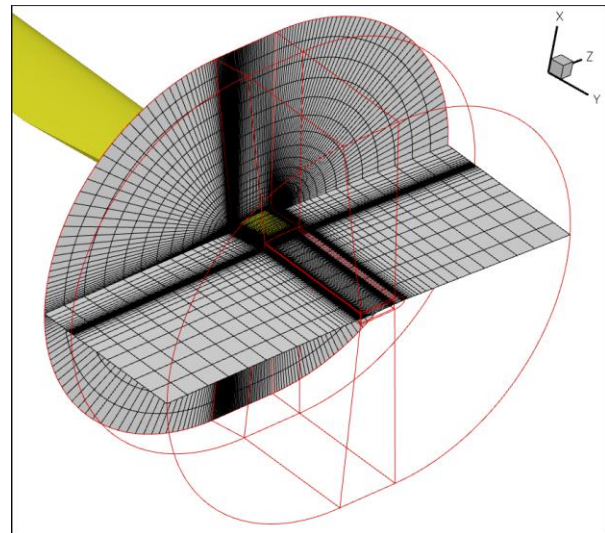Fig 3. Background grid component



Fig 4. Root grid component

The region of the blade root (fig. 4) is meshed using O-type grid in stream-wise and H-type grid in crosswise directions. It spans from the surface for 2 chord lengths (0.88 m) in the normal direction and 1.5 chords (0.66 m) in the radial direction. It consist of 13 blocks and 1.19 ·10$^6$ volumes per blade. The majority of the blade is covered by the blade centre (fig. 5) chimera grid component of a C-type in streamwise and H-type in crosswise directions. It spans from the surface for 2 chord lengths (0.88 m) in the normal direction and consist of 118 blocks and 5.30·10$^6$ volumes per blade. The close-up reveals the geometrical complexity of the mesh and block topology near the trimming tab at the trailing edge of the blade. The last component grid covers the area of blade tip (fig. 6). Due to rounded tip shape the O-type grid type is applied in streamwise and crosswise directions. It spans from the surface for 2 chord lengths (0.88 m) in the normal direction and consist of 19 blocks and 1.08 ·10$^6$ volumes per blade. The close-up presents a rounded tip surface mesh in more details.
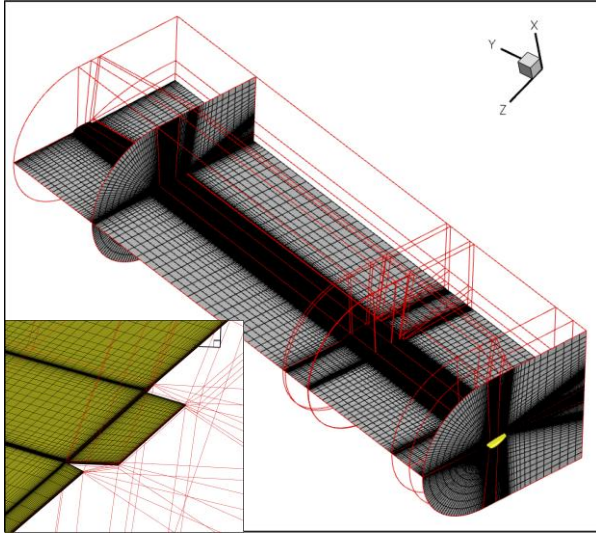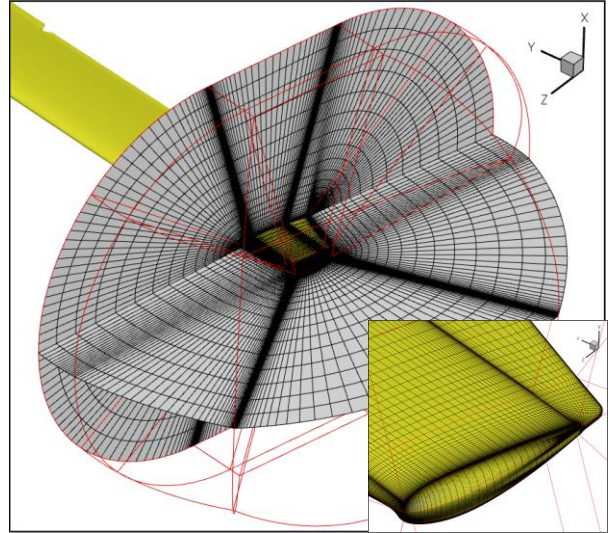
Fig 5. Centre grid component



Fig 6. Tip grid component

The root, centre and tip components (and the "hole") undergo all prescribed motions: translation with forward flight velocity, rotation around the azimuth $\psi$, a constant tilt by a shaft angle $\gamma$, unsteady pitch ($\theta(\psi)$)) and flap ($\beta(\psi)$)). The non-dimensional distance of the first point from the solid surfaces $y^+$ is of the order of 1.0 for all grids. The complete set of meshes consists of 632 blocks and 40.6 millions of control volumes and is integrated within the FLOWer solver using chimera technique (fig. 7).
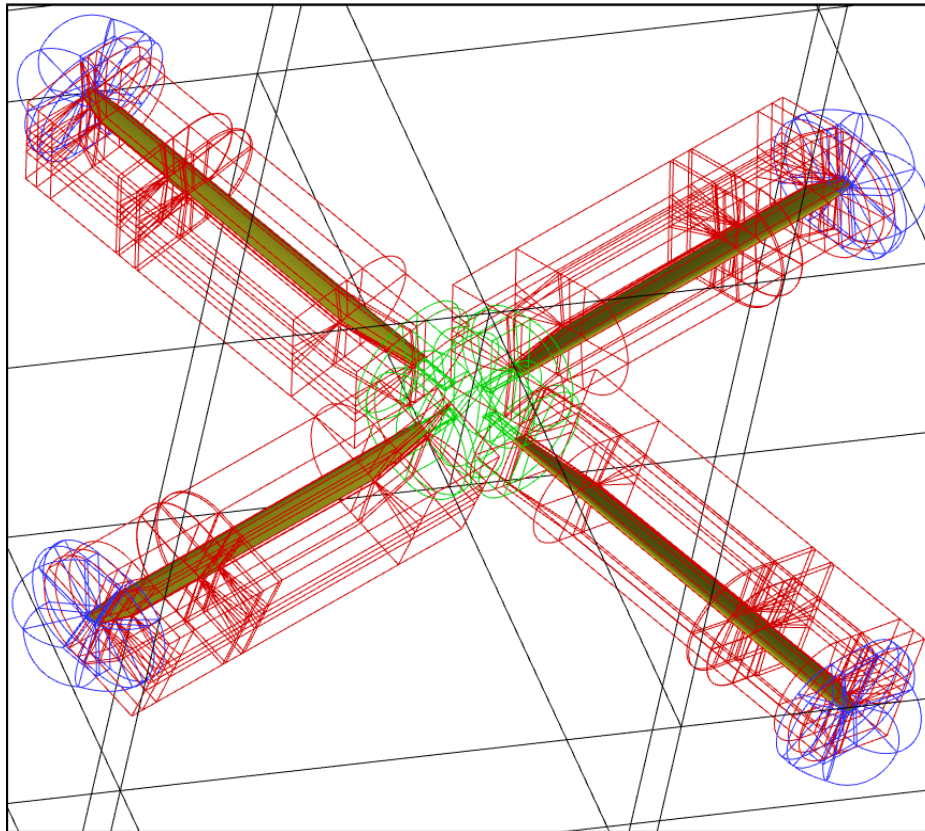


Fig 7. Chimera overlapping grid topology (black colour – background, red colour – blade centre, green colour – blade root, blue colour – blade tip)

The blade component grids (root – green colour, centre – red colour and tip – blue colour) for the first blade together with a blade "hole" are placed in the background grid (black colour). The remaining three blades are set-up and managed by the flow solver FLOWer. As a result the complete project consisting of all 4 blades is ready for the numerical simulation.

## PHYSICAL AND NUMERICAL MODELLING

The present investigation was carried out with the FLOWer solver from DLR (Kroll et al., 2002). It is a modern, parallel, block-structured, cell-centred code solving Favre-averaged Navier-Stokes equations (RANS) with various turbulence models. The ROT version of the code allows usage of a chimera overlapping grids technique and moving meshes. From the various turbulence closures implemented in FLOWer, the two-equation, low-Reynolds $k$-$\omega$ turbulence model of LEA (Linear Explicit Algebraic Stress Model) was chosen (Rung et al., 1999). The LEA $k$-$\omega$ model provides two additional transport equations for the specific kinetic turbulence energy $k$ and the specific dissipation rate $\omega$. It represents the linear part of a non-linear explicit algebraic stress model casted in terms of the Wilcox $k$-$\omega$ formulation. It combines the advantages of Reynolds stress modelling accuracy with the numerical advantages of the eddy viscosity concept. The URANS equations require additional relations in order to form a closed set. For the equation of state the perfect gas law is used with the specific heat ratio $\gamma = 1.4$, gas constant $R = 287.1$, Prandtl number $Pr = 0.72$ and turbulent Prandtl number $Pr_t = 0.9$. The laminar viscosity is calculated according to Sutherland's law binding viscosity to the temperature field. The summary of physical modelling in FLOWer may be found in tab. 3.

| physical model: | unsteady Favre-averaged Navier-Stokes equations (URANS) |
|---|---|
| turbulence model: | LEA $k$-$\omega$ |
| gas model: | perfect gas |

Tab. 3 Physical modelling in FLOWer code

The numerical algorithm uses a semi-discrete approach, utilizing a 2$^{nd}$ order finite-volume formulation for spatial discretisation and a 2$^{nd}$ order implicit dual-time-stepping (with explicit 5-stage Runge-Kutta) method for integration in time. In order to increase the convergence rate, the local time stepping and the implicit residual averaging techniques are included. Additionally, the three-grid multigrid strategy with V-cycles is used. To damp numerical oscillations the scalar artificial dissipation model of Jameson is implemented. The summary of numerical modelling in FLOWer may be found in tab. 4.

| space discretization: | finite volume method (2$^{nd}$ order) |
|---|---|
| temporal discretization: | dual-time-stepping + Runge-Kutta (2$^{nd}$ order) |
| artificial dissipation: | JST switch (scalar) |
| convergence acceleration techniques: | local time stepping, implicit residual smoothing, multigrid |
| grid type: | chimera overlapping |

Tab. 4 Numerical modelling in FLOWer code

Using a time step equal to the time needed for a rotation by 0.25$^{o}$ degrees of azimuth (1440 time steps per period) and a CFL number $\leq 10.0$ for internal R-K stages the dual time-

stepping scheme gained a drop of residuals by 3.0 orders of magnitude within couple of iterations, which proved to be sufficient to obtain accurate unsteady flow field around rotor (tab. 5).

| | |
|---|---|
| time step [$^o$]: | 0.25 |
| CFL: | ≤10.0 |
| residual reduction: | $10^{-3}$ |

Tab. 5 Common numerical parameters

## BOUNDARY CONDITIONS AND BLADE MOTION

The project contains three types of boundary conditions: solid no-slip wall applied at the rotor blades (root, centre and tip component grids), far-field with velocity equal to 0 (outer edge of the background component grid) and special chimera boundary condition (outer edge of the root, centre and tip component grids) designed for interpolation of flow data between meshes.

The low-speed 99.0 km/h flight (flight 6522, state 29) was realized at 918.4 m above the sea level in the temperature of 3.4 C. The rotor operated at 28.00 rad/s in a plane almost parallel to the ground. At this flight condition pilots report significantly increased level of vibration and noise which is believed to be due to the strong Blade-Vortex Interactions (BVIs). The ambient air density has been obtained from the standard atmosphere model (1.143 kg/m$^3$). The resulting tip and flight Mach and Reynolds numbers are summarized in tab. 6.

| | |
|---|---|
| tip Mach number $Ma_T$: | 0.6593 |
| tip Reynolds number $Re_T$: | $6.38 \cdot 10^6$ |
| forward flight Mach number $Ma_\infty$: | 0.0825 |
| forward flight Reynolds number $Re_\infty$: | $0.8 \cdot 10^6$ |
| advance ratio $Ma_\infty/Ma_T$ $\mu$: | 0.125 |
| atmospheric density $\rho_{atm}$ [kg/m$^3$] : | 1.143 |
| atmospheric temperature $T_{atm}$ [K]: | 276.55 |
| dynamic viscosity $\mu_{atm}$ [kg/m/s]: | $1.73 \cdot 10^{-5}$ |
| eddy viscosity ratio $\mu_T/\mu_{atm}$: | 0.001 |
| turbulence level $Tu$: | 0.005 |

Tab. 6 Boundary conditions - low-speed forward flight (flight 6522, state 29)

The high-speed 265.6 km/h test flight (flight 6522, state 53) was realized at 931.0 m above the sea level in the temperature of 5.2 C. The rotor operated again at 28.00 rad/s. The high forward speed of a helicopter was set above the suggested limit of velocity called "never exceed" in flight ($V_{ne}$ = 260 km/h for the PZL W3-A "Sokół" (Falcon) helicopter). The ambient air density has been obtained from the standard atmosphere model (1.134 kg/m$^3$). The resulting tip and flight Mach and Reynolds numbers are summarized in tab. 7. The additional transport equations require specification of the inlet characteristics of turbulence. The default far-field values of eddy viscosity ratio and turbulence level are used for all simulations ($\mu/\mu_T$ = 0.001 and $Tu$ = 0.005).

During the test flight the control angles has been recorded as the blade pitching angle $\theta(\psi)$, flapping angle $\beta(\psi)$ around the hinge (located at z = 0.14 m) and constant shaft normal plane tilt $\gamma$ according to the flight direction. The harmonics can be analytically described for low-speed flight (flight 6522, state 29) by eqn. (2):

$$\theta\,[^{\circ}] = 16.01 + 1.58 \cos(\psi) - 5.11 \sin(\psi),$$
$$\beta\,[^{\circ}] = 3.55 - 0.62 \cos(\psi) - 0.63 \sin(\psi), \qquad (2)$$
$$\gamma\,[^{\circ}] = -0.32.$$

and for high-speed flight (flight 6522, state 53) by eqn. (3):

$$\theta\,[^{\circ}] = 21.01 + 1.95 \cos(\psi) - 10.52 \sin(\psi),$$
$$\beta\,[^{\circ}] = 3.75 - 0.47 \cos(\psi) + 0.64 \sin(\psi), \qquad (3)$$
$$\gamma\,[^{\circ}] = -8.26.$$

It is assumed that the angle of $0^{\circ}$ of pitch is referring to the inflow angle of $0^{\circ}$ due to rotation at the root location of the blade. In this convention the tip of the blade is rotated nose-down by $-12^{\circ}$ due to blade linear twist.

| | |
|---|---|
| tip Mach number $Ma_T$: | 0.6572 |
| tip Reynolds number $Re_T$: | $6.30 \cdot 10^6$ |
| forward flight Mach number $Ma_\infty$: | 0.2206 |
| forward flight Reynolds number $Re_\infty$: | $2.11 \cdot 10^6$ |
| advance ratio $Ma_\infty/Ma_T$ $\mu$: | 0.336 |
| atmospheric density $\rho_{atm}$ [kg/m$^3$] : | 1.134 |
| atmospheric temperature $T_{atm}$ [K]: | 278.35 |
| dynamic viscosity $\mu_{atm}$ [kg/m/s]: | $1.74 \cdot 10^{-5}$ |
| eddy viscosity ratio $\mu_T/\mu_{atm}$: | 0.001 |
| turbulence level $Tu$: | 0.005 |

Tab. 7 Boundary conditions - high-speed forward flight (flight 6522, state 53)

**LOW-SPEED FORWARD FLIGHT RESULTS**

In the current analysis the rotor moves with the forward flight Mach number $Ma_\infty$ in the direction opposite to the z-axis and rotates with the tip Mach number $Ma_T$ around the direction tilted forward from the vertical x-axis by a constant shaft angle $\gamma$. For the post-processing purposes the forward movement and the shaft normal plane inclination $\gamma$ are removed from the plots. At $\psi = 0^{\circ}$ the first rotor blade is pointing in the backward direction.

The flow-field around the rotor in low-speed forward flight (advance ratio $\mu = 0.125$) is visualised by streamlines and a constant vorticity surface in fig. 8. It is evident that the incoming air is strongly deflected towards the ground. It is an intermediate flow condition between hover (perpendicular flow through the disc) and high-speed forward flight (almost parallel flow through the disc and wake convection). The blade tip and trimming tabs create strong vortices that interact with the blades creating a dominating state of the classical (perpendicular) blade-vortex interaction (BVI) for each azimuthal location of the blade. A very dangerous (vibration, pilot control) and unpleasant (impulsive noise) state for the rotor.

Fig. 9 and 10 present a contour map of pressure coefficient $Ma^2 C_P$ and areas of reversed flow based on the change of sign of the skin friction coefficient $Ma^2 C_F$ for the blade surface in steps of $30^{\circ}$ of rotation. The pressure coefficient $Ma^2 C_P$ and skin friction coefficient $Ma^2 C_F$ are defined with:

$$Ma^2 C_P = \frac{p - p_{atm}}{\frac{1}{2}\rho_{atm} a_{atm}^2}, \qquad Ma^2 C_F = \frac{\tau}{\frac{1}{2}\rho_{atm} a_{atm}^2}, \qquad (4)$$

where $p$ - is static pressure and $\tau$ - wall shear stress. Eqn. (4) contains also atmospheric conditions in flight: pressure $p_{atm}$, density $\rho_{atm}$, and speed of sound $a_{atm}$.
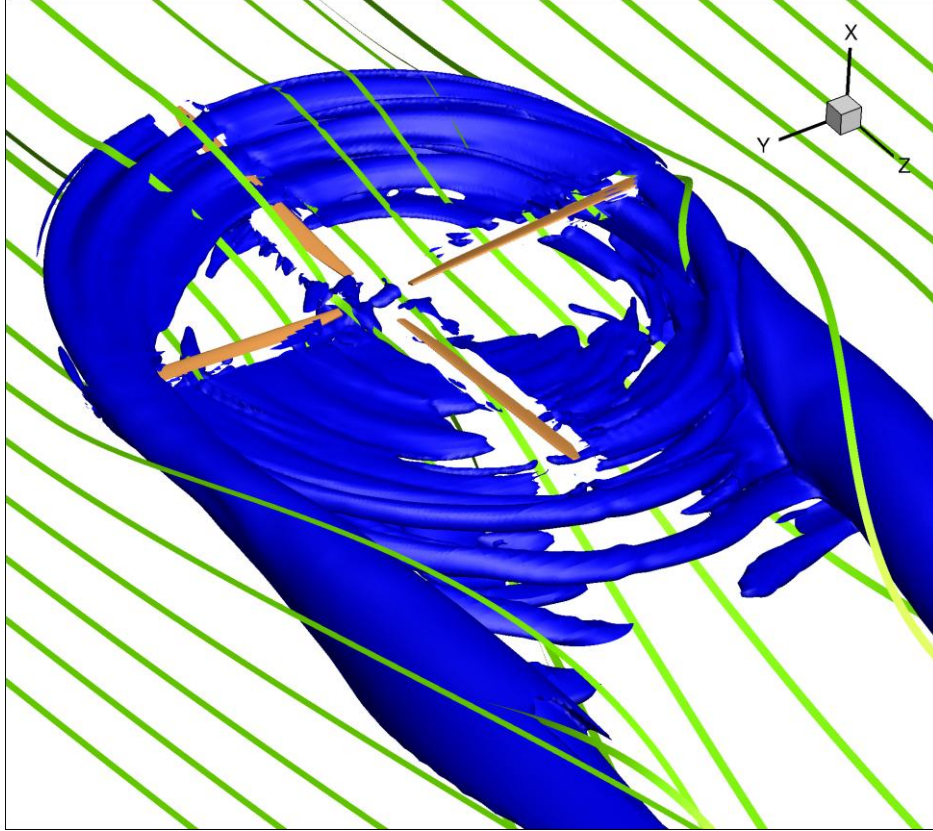


Fig. 8 Aerodynamic wake (iso-vorticity surface) - low-speed forward flight (flight 6522, state 29)

Due to the low forward speed of the rotor the pressure coefficient $Ma^2 C_P$ at the outer part of the blade is almost indistinguishable for different azimuthal positions $\psi$ of the blade (fig. 9). On the retreating side, near the root, there is an area of high pressure connected with the local reversed flow direction and possibly separation between $\psi = 150^o$ and $\psi = 270^o$ (marked by red color in fig. 10). This kind of visualization cannot distinguish between areas of boundary layer separation and reversed air flow due to the forward flight specific inflow conditions on the retreating side of the rotor. It is worth mentioning that even for a low inflow velocity which occurs on the retreating side there still exist areas of supersonic flow and weak shock waves near the tip due to the high local angle of attack, which cause small separation bubbles. It is visible in fig. 10 as a small red area located close to the leading edge (near the tip) of the retreating blades.

Because the chimera technique allows overlapping of more than one mesh on the surface of the body the calculation of the aerodynamic forces acting on this surface may lead to wrong predictions. Due to existence of multiple volumes in one region on the surface it is necessary to remove the overlapping by creation of the unique surface of the rotor. The special post-processing tool Trisurf (DLR) removes the overlapping on the surface and

calculates properly all aerodynamic forces acting on the rotor blades. It is performed in the post-processing phase.
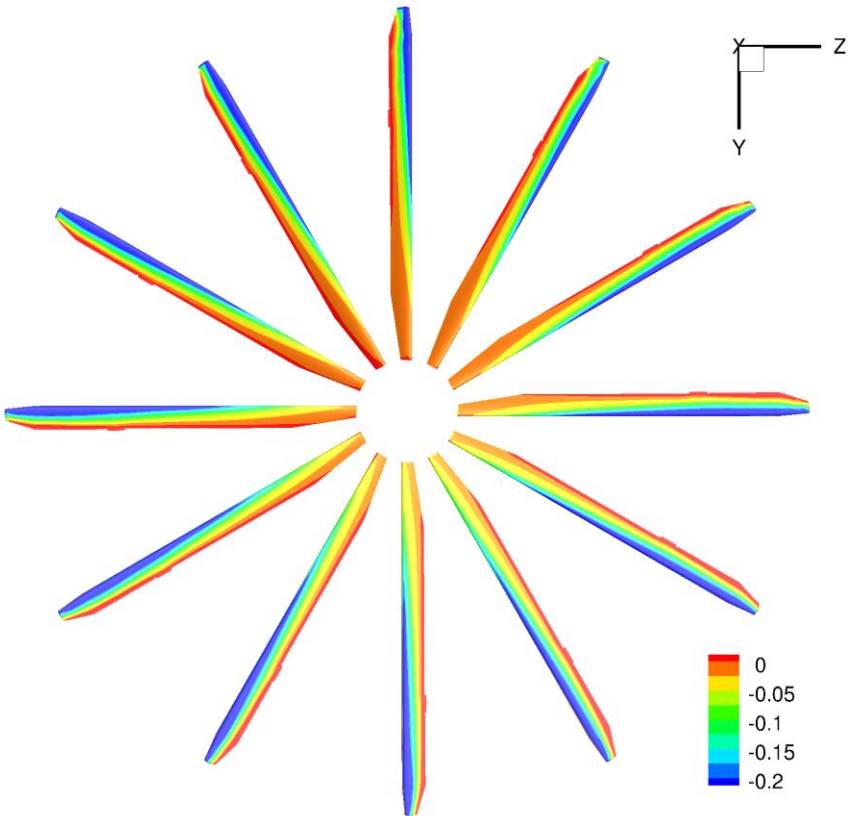


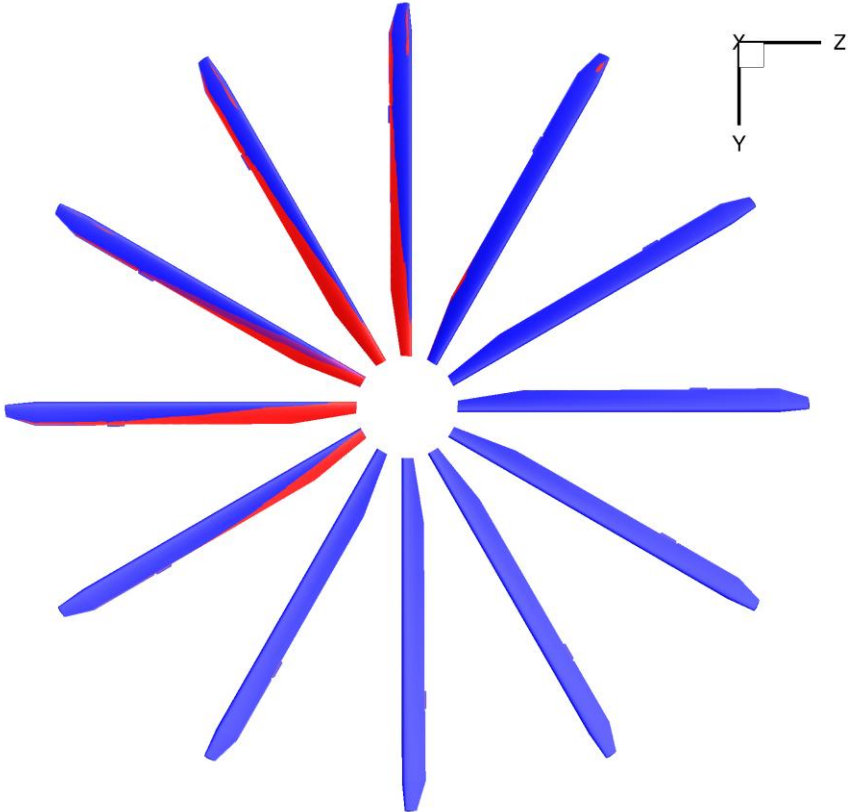Fig. 9 Pressure coefficient $Ma^2C_P$ – low-speed forward flight (flight 6522, state 29)



Fig. 10 Sign of skin friction coefficient $Ma^2C_F$ – low-speed forward flight (flight 6522, state 29)

Fig. 11 contains a change in time of the thrust coefficient $C_T$ and power coefficient $C_P$ (for the last period of rotation) defined with relations:

$$C_T = \frac{F_X}{\rho_{atm} A U_T^2}, \qquad C_P = \frac{M_X}{\rho_{atm} A U_T^3}, \qquad (5)$$

in which $F_X$ i $M_X$ are component of total force acting along the shaft (x-axis) and total moment around the shaft (x-axis), $\rho_{atm}$ - atmospheric density, $A = \pi R^2$ - rotor disc area and $U_T$ - tip speed in hover. The time history of thrust $C_T$ and power $C_P$ coefficients contains forces and moments due to pressure and friction with overlapping of the grids removed from the surface. It is evident that the values fluctuate in time with an amplitude of ~5 % for $C_T$ and ~6% for $C_P$ and constant means equal to $\overline{C}_T = 0.00676$ and $\overline{C}_P = 0.000369$ (tab. 8).

| $\overline{C}_T:$ | 0.00676 |
|---|---|
| $\overline{C}_P:$ | 0.000369 |

Tab. 8 Mean thrust coefficient $\overline{C}_T$ and power coefficient $\overline{C}_P$ - low-speed forward flight (flight 6522, state 29)

The mean component of the force acting against the weight of the helicopter is equal to 72289 N (7369 kg), mean shaft moment is equal to 30976 Nm and power required to turn the shaft is equal to 867 kW (1195 HP). It is worth to mention that the PZL W3-A "Sokół" (Falcon) helicopter had a take-off weight of 6100 kg and was equipped with engines of the total power equal to 1800 HP. The CFD calculation over predicts the mean force acting against the weight of the helicopter by 21%. The mean power required to turn the shaft is equal to 66% of the total available power of the engines.
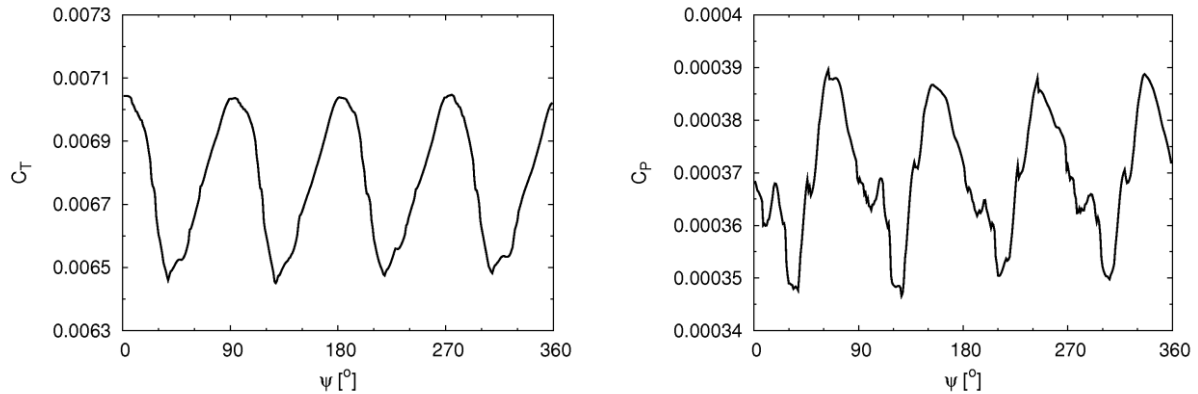


Fig. 11 Time variation of thrust coefficient $C_T$ and power coefficient $C_P$ - low-speed forward flight (flight 6522, state 29)

## HIGH-SPEED FORWARD FLIGHT RESULTS

The advancing blade of the PZL W3-A "Sokół" (Falcon) helicopter in high-speed forward flight experiences an increase of the local inflow velocity leading to the reduction of the pitch angle of the blade down to the value at the tip close to $0^o$ (or even negative) at the azimuthal position of $\psi = 90^o$. By this method of control the supersonic flow areas are limited, but shock waves still exist, having a strong impact on the flow losses and generated noise. On the other hand, the retreating blade experiences a deficiency of the inflow velocity resulting in the local

increase of the pitch angle up to the value at the tip close to $20^o$ at the azimuthal position of $\psi = 270^o$. It may procure boundary layer separation and dynamic stall of the blades. Compressibility effects due to strong shock-wave boundary layer interaction on the advancing side and separation leading to dynamic stall on the retreating side of the rotor are two main limiting phenomenon for a rotor in high-speed forward flight.

The flow-field around the rotor in high-speed forward flight (advance ratio $\mu = 0.336$) is visualised by streamlines and a constant vorticity surface in fig. 12.
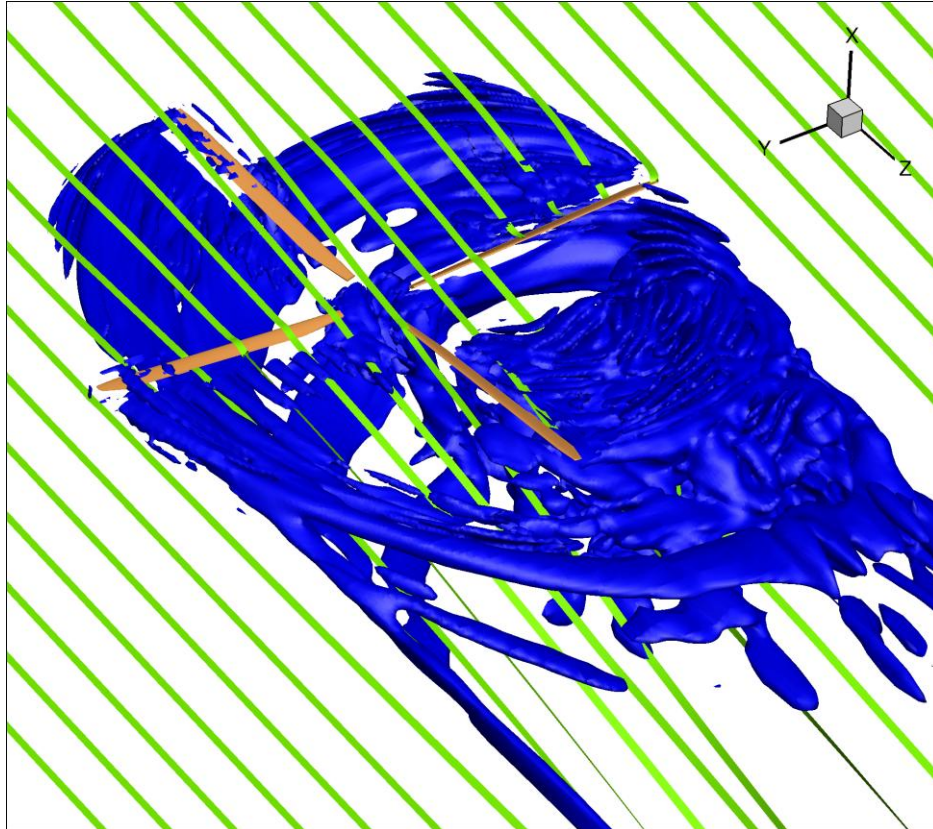


Fig. 12 Aerodynamic wake (iso-vorticity surface) - high-speed forward flight (flight 6522, state 53)

The rotor wake is deflected mildly towards the ground and convected strongly in the downstream direction. The blade tip and trimming tabs create strong vortices that interact with the blades leading to the perpendicular and parallel blade-vortex interactions (BVI) for different azimuthal locations $\psi$ of the blade. In the computed state very strong vortical structures emerge as the effect of the separation of boundary layer on the retreating side (third quadrant) of the rotor leading to the dynamic stall phenomenon.

Fig. 13 and 14 present a contour map of pressure coefficient $Ma^2C_P$ and areas of reversed flow based on the change of sign of the skin friction coefficient $Ma^2C_F$ for the blade surface in steps of $30^o$ of rotation. Due to the high forward speed of the rotor the contour map of pressure coefficient $Ma^2C_P$ is highly asymmetrical for different azimuthal positions $\psi$ of the blade (fig. 13). On the retreating side, near the root, there exist an area of high pressure connected with the local reversed flow direction and possibly separation between $\psi = 180^o$ and $\psi = 300^o$ (marked by red color in fig. 14) spanning for almost the whole length of the blade, excluding just the tip area. Again, this kind of visualization cannot distinguish between areas of boundary layer separation and reversed air flow due to the forward flight specific inflow conditions on the retreating side of the rotor. Due to high relative inflow velocity at the

blade tip on the advancing side large areas of supersonic flow emerge terminated by shocks waves, with increasing strength towards the tip.
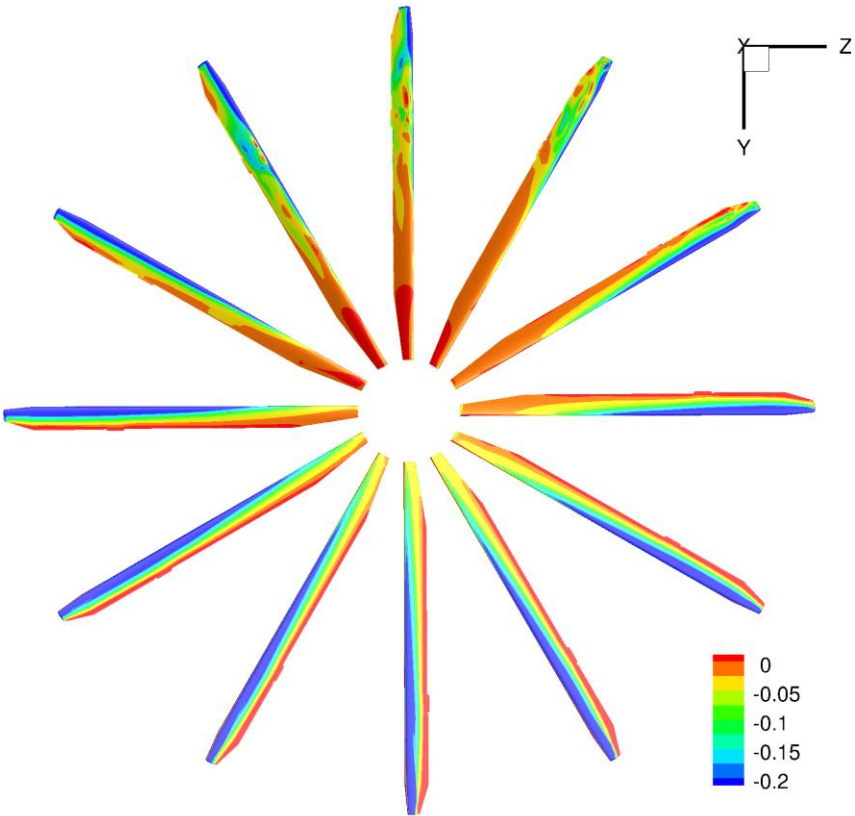


Fig. 13 Pressure coefficient $Ma^2 C_P$ – high-speed forward flight (flight 6522, state 53)
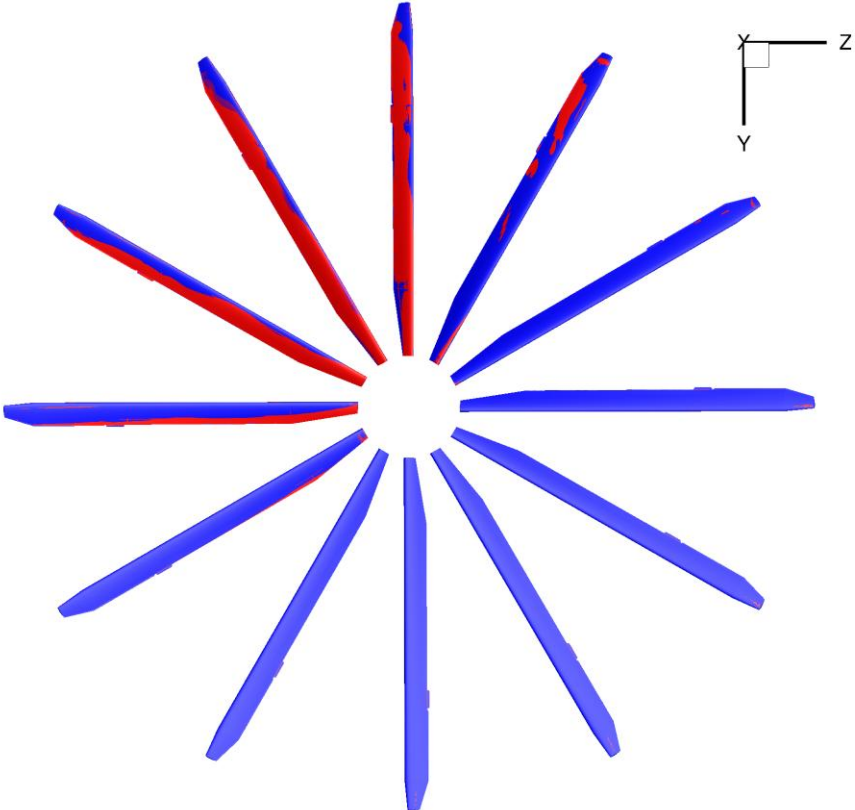


Fig. 14 Sign of skin friction coefficient $Ma^2 C_F$ – high-speed forward flight (flight 6522, state 53)

Low angle of attack blocks the flow from boundary layer separation at this location and the flow remains fully attached (fig. 14). On the other hand, on the retreating side the blade is subjected to high incidence, hence causing strong acceleration near the leading edge with small supersonic areas and weak shocks leading to mild boundary layer separation. It is visible in fig. 14 as small red areas located close to the leading edge (near the tip) of retreating blades.

Fig. 15 contains a change in time of the thrust coefficient $C_T$ and power coefficient $C_P$ (for the last period of rotation). The time history of thrust $C_T$ and power $C_P$ coefficients contains forces and moments due to pressure and friction with overlapping of the grids removed from the surface. It is evident that the values fluctuate in time with an amplitude of ~6% for $C_T$ and ~10% for $C_P$ and constant means equal to $\overline{C}_T = 0.00666$ and $\overline{C}_P = 0.000705$ (tab. 9).

| | |
|---|---|
| $\overline{C}_T$ : | **0.00666** |
| $\overline{C}_P$ : | **0.000705** |

Tab. 9 Mean thrust coefficient $\overline{C}_T$ and power coefficient $\overline{C}_P$ - high-speed forward flight (flight 6522, state 53)

The mean component of the force acting against the weight of the helicopter is equal to 69919 N (7127 kg), mean shaft moment is equal to 58709 Nm and power required to turn the shaft is equal to 1644 kW (2266 HP). It is worth to mention that the PZL W3-A "Sokół" (Falcon) helicopter had a take-off weight of 6100 kg (minus 150 kg of fuel consumed between states 29 and 53) and was equipped with engines of the total power equal to 1800 HP. The CFD calculation over predicts the mean force acting against the weight of the helicopter by 20%. The mean power required to turn the shaft is equal to 126 % of the total available power of the engines.
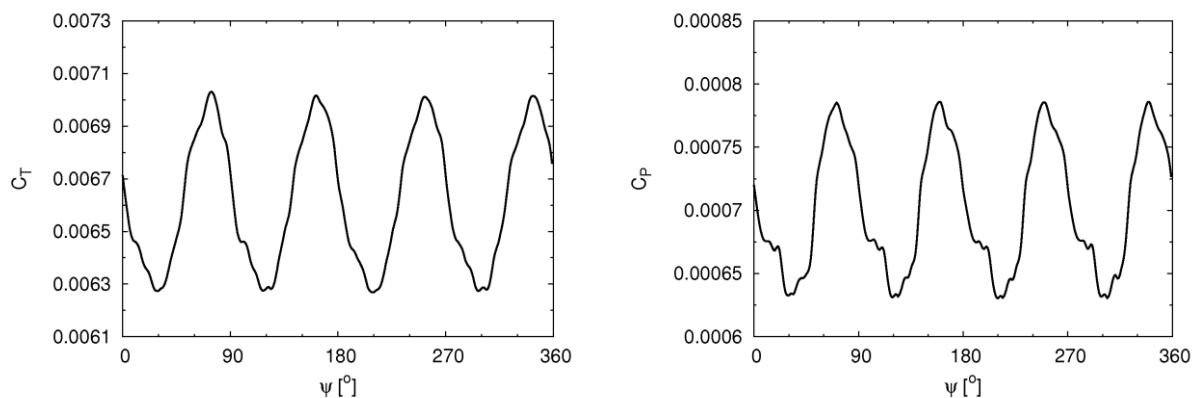


Fig. 15 Time variation of thrust coefficient $C_T$ and power coefficient $C_P$ - high-speed forward flight (flight 6522, state 53)

## CONCLUSIONS

The numerical simulation of flow past the isolated rotor of the PZL W3-A "Sokół" (Falcon) helicopter in low-speed and high-speed forward flight (flight 6522, states 29 and 53) leads to a significant overprediction of the mean thrust force by ~20 %. Moreover, the power required to turn the shaft is also overpredicted for the high-speed test case. The stability of the rotor is not achieved - the residual longitudinal and lateral forces and moments do not balance. The possible explanation is that the real blades are not stiff, but relatively flexible – they do bend and twist under loads (see fig. 1), which usually reduces the effective inflow velocity and angle of attack, which as a result lowers the lift and drag of the blade sections.

On the other hand, the influence of the fuselage, tail rotor, rotor head etc. is not taken into account. Finally, there is no trimming procedure of the rotor in the numerical simulation. The calculation is based on the values of control angles recorded during flight tests. Taking into account all simplifications in the numerical model the limited comparison with flight test data is acceptable.

## ACKNOWLEDGEMENTS

## REFERENCES

Doerffer P., Szulc O., (2010): *Obliczeniowa analiza aeroakustyczna dwóch wirników nośnych śmigłowca. Wirnik 4-łopatowy oparty na profilach NACA. Opracowanie modelu geometrycznego, generacja siatki obliczeniowej, wykonanie obliczeń testowych,* Opracowanie wewnętrzne IMP PAN 245/2010.

Doerffer P., Szulc O., (2011): *Obliczeniowa analiza aeroakustyczna dwóch wirników nośnych śmigłowca. Wirnik 4-łopatowy oparty na profilach NACA. Obliczenia numeryczne opływu wirnika w locie poziomym z małą i dużą prędkością,* Opracowanie wewnętrzne IMP PAN 18/2011.

IGG: Interactive Geometry Modeler and Grid Generator from Numeca International (2012): Retrieved May 22, from  http://www.numeca.com/index.php?id=72

Kania W.,  Stalewski W., (2000): *Development of new generation main and tail rotors blade airfoils*, Proceedings of the 22nd Congress of the International Council of the Aeronautical Sciences, Harrogate (United Kingdom)

Kroll N., Rossow C. C., Schwamborn D., Becker K., Heller G., (2002): *MEGAFLOW – a numerical flow simulation tool for transport aircraft design*, Proceedings of the 23rd Congress of the International Council of the Aeronautical Sciences, Toronto (Canada)

Rung T., Lübcke H., Franke M., Xue L., Thiele F., Fu S., (1999): *Assessment of explicit algebraic stress models in transonic flows*, Proceedings of the 4th International Symposium on Engineering Turbulence Modelling and Measurements, Corsica (France)

Schwarz T. (2005): *The overlapping grid technique for the time accurate simulation of rotorcraft flows*, Proceedings of the 31st Rotorcraft Forum, Florence (Italy)